npj | computational materials

Article

Published in partnership with the Shanghai Institute of Ceramics of the Chinese Academy of Sciences

https://doi.org/10.1038/s41524-026-02007-y

Multiscale investigation of thermal transport in β-Ga_2O_3-based heterointerfaces enabled by machine learning potential: cross-scale parameter

Zhanpeng Sun[1,2,3,4,7], Zijun Qi[1,2,3,4,7], Yunfei Song[1,2,5], Lijie Li[6], Sheng Liu[1,2,3,5], Wei Shen[1,2,3,4,5] ✉ & Gai Wu[1,2,3,4,5] ✉

The rising power density of advanced electronics demands improved thermal management, while traditional single-scale methods are unable to fully reveal the complex heat transfer mechanisms in heterostructures. This work establishes a multiscale simulation framework by constructing a machine learning potential, enabling accurate cross-scale parameter transfer from atomic to mesoscopic and then to macroscopic levels. Results show that the thermal boundary resistance (TBR) at the β-Ga_2O_3/diamond interface is higher than that at the β-Ga_2O_3/Si and β-Ga_2O_3/SiC interfaces, and that the TBR decreases with increasing temperature, which contradicts conventional understanding. Vibrational density of states and interface conductance modal analysis elucidate the underlying mechanisms. These mesoscale insights are incorporated into macroscopic simulations, showing the β-Ga_2O_3/diamond heterostructure's peak power capability reaches 226% of that of β-Ga_2O_3/Si. Further analysis reveals that although the thermal conductivity of the heat-spreading substrate remains the dominant factor in overall thermal performance, the thermal bottleneck gradually shifts toward the interface as both substrate conductivity and operating temperature rise. Moreover, crystal orientation significantly influences thermal performance and thermal stress distribution, necessitating careful trade-offs. This study not only provides effective strategies for optimizing β-Ga_2O_3-based devices but also establishes a generalizable paradigm for cross-scale thermal management research in heterogeneous material systems.

The continuous trend toward miniaturization, higher performance, and greater integration in electronic technologies has led to a rapid increase in the power density of electronic components. Consequently, effective thermal management within electronic systems and devices has become a critical bottleneck limiting their performance enhancement and reliability[1–4]. Heat transfer is a complex physical process that involves multiple spatial and temporal scales, particularly in interfacial heat transfer within heterostructures. The thermal performance of electronic devices is ultimately determined by a combination of factors across scales, including phonon elastic and inelastic scattering at the atomic level[5], interfacial thermal transport and diffusive-ballistic heat transfer at the mesoscopic scale[6], and the coupling of heat distribution with thermal stresses at the macroscopic level[7]. Early studies primarily focused on individual scales, and achieving cross-scale parameter transfer for multiscale thermal management research remains a significant challenge. Therefore, developing multiscale thermal transport simulation methods capable of bridging microscopic mechanisms, mesoscopic phenomena, and macroscopic responses has become an urgent need in thermal management research for advanced electronic materials and devices.

In recent years, several studies have enabled cross-scale coupled multiscale simulations by incorporating parameters, including thermal

[1]School of Integrated Circuits, Wuhan University, Wuhan, China. [2]The Institute of Technological Sciences, Wuhan University, Wuhan, China. [3]Wuhan University Shenzhen Research Institute, Shenzhen, China. [4]Hubei Key Laboratory of Electronic Manufacturing and Packaging Integration, Wuhan University, Wuhan, China. [5]School of Power and Mechanical Engineering, Wuhan University, Wuhan, China. [6]College of Engineering, Swansea University, Swansea, UK. [7]These authors contributed equally: Zhanpeng Sun, Zijun Qi. ✉e-mail: wei_shen_@whu.edu.cn; wugai1988@whu.edu.cn

conductivity, coefficient of thermal expansion (CTE), and thermal boundary resistance (TBR), derived from first-principles calculations at the microscopic scale and molecular dynamics (MD) simulations at the mesoscopic scale into macroscopic finite element (FE) analyses[8–10]. However, these studies still face challenges in transferring parameters from the microscopic to the mesoscopic scale, limiting the integration of mechanistic insights across scales. This limitation arises because the parameters derived from the microscopic scale are independent of those obtained from the mesoscopic scale. Furthermore, the accuracy of mesoscopic-scale MD simulations heavily depends on the quality of the interatomic potential used[11]. However, it is challenging for traditional potentials to achieve the accuracy of first-principles calculations[12]. This discrepancy results in a mismatch in accuracy between parameters derived from the microscopic scale and those from the mesoscopic scale, ultimately undermining the reliability of macroscopic FE simulations. Fortunately, driven by advances in artificial intelligence, machine learning potentials (MLPs) trained on datasets generated from density functional theory (DFT) calculations are emerging as powerful tools in materials science[11]. MLPs enable MD simulations to achieve accuracy comparable to that of DFT while maintaining high computational efficiency, particularly in the study of interfacial thermal transport[13–17], thereby offering a promising pathway to bridge the microscopic and mesoscopic scales. MLPs are trained on atomic energies and forces obtained from first-principles calculations at the microscopic scale. Subsequently, MD simulations at the mesoscopic scale, performed using these MLPs, generate results with accuracy comparable to that of first-principles computations. These results are then used as input parameters for macroscopic FE analysis, enabling a multiscale transfer of information from the microscopic to the mesoscopic and ultimately to the macroscopic level. Among various MLPs, the neuroevolution potential (NEP) stands out in atomic simulations for interface heat transfer applications due to its higher accuracy and lower computational cost. NEP can be implemented via GPUMD (Graphics Processing Unit MD)[18,19].

Gallium oxide (Ga_2O_3) is an ultrawide-bandgap semiconductor that exhibits significant potential for high-power electronic devices due to its large bandgap, high Baliga's figure of merit, and exceptionally high critical breakdown electric field[20–22]. However, the room-temperature average thermal conductivity of Ga_2O_3 is only around 15 $W{\cdot}m^{-1}{\cdot}K^{-1}$, which significantly limits its applicability in high-power electronic devices[23,24]. A promising approach to enhance heat dissipation is to construct a heterostructure by integrating Ga_2O_3 with a high thermal conductivity material serving as a heat-dissipating substrate[25]. However, the thermal performance of heterostructures depends not only on the thermal conductivity of the heat sink but also critically on the TBR. Consequently, single-scale studies are insufficient to fully capture the thermal management mechanisms in Ga_2O_3-based devices. This underscores the necessity of a comprehensive multiscale study of thermal transport in Ga_2O_3-based heterostructures.

In this work, an NEP has been developed based on a first-principles-derived training dataset, enabling the simulation of interfacial heat transfer in β-Ga_2O_3/substrate heterostructures with substrates including silicon (Si), silicon carbide (SiC), and diamond. The MLP serves as an effective bridge, transferring atomic-scale quantities, such as atomic energies and forces from first-principles calculations to mesoscopic-scale MD simulations, thereby enabling MD to achieve accuracy comparable to that of DFT methods. Subsequently, mesoscopic parameters derived from MD, including TBR and thermal conductivity, are used as input for macroscopic FE simulations. This approach establishes a multiscale framework for thermal transport simulation, spanning from the microscopic to the mesoscopic and ultimately to the macroscopic scale, as shown in Fig. 1. The thermal management of β-Ga_2O_3-based heterostructures has been systematically investigated using this multiscale approach. Finally, a cross-scale analysis and understanding of the performance differences among various β-Ga_2O_3-based heterostructures are achieved through vibrational density of states (VDOS), phonon participation ratio (PPR), and interface conductance modal analysis (ICMA). This study not only provides valuable optimization strategies for thermal management in β-Ga_2O_3-based systems, but also lays the foundation for multiscale investigations of thermal management in other materials.

Results

Atomic-scale dataset construction and machine learning performance evaluation

The training dataset primarily consists of two components: bulk structures and interface structures, as illustrated in Fig. 2a. The bulk crystal structures include supercells of β-Ga_2O_3, Si, SiC, and diamond, while the interface structures comprise β-Ga_2O_3/Si, β-Ga_2O_3/SiC, and β-Ga_2O_3/diamond. The temperature range is set from 10 to 1000 K, with appropriate atomic displacements and strains applied to some structures. The initial interfacial distances for the interface structures in the training dataset are determined through extensive testing, as shown in Fig. 2c–f. The interfacial energies of different interface combinations at various interfacial distances are calculated, and the most stable interfacial distance for each system is used to construct the corresponding interface structures in the training dataset. Finally, 2400 structures are used as the training dataset and 1200 structures are used as the test dataset. More detailed information on the training dataset and training hyperparameters can be found in the methods section. The loss functions for energy, forces, and virial are shown in Fig. 2b. After 1,000,000 iterations, the relevant parameters in both the training and test datasets exhibit clear convergence. To provide a clearer assessment of the NEP accuracy, Fig. 2g–i compares the energies, forces, and virial stresses predicted by the NEP with the corresponding DFT calculations on the training and test datasets; the error distributions for the predicted energy, forces, and virial stresses are illustrated in Fig. 2j–l. In Fig. 2g, the energy clustered into different groups corresponds to different bulk and interface structures. The root-mean-square errors (RMSEs) for energy on the training and test datasets are 4.9 meV/atom and 4.8 meV/atom, respectively; for forces, the RMSEs are 229.0 meV/Å and 212.2 meV/Å, respectively; and for virial stresses, the RMSEs are 37.2 meV/atom and 34.4 meV/atom, respectively. In this work, the RMSE value of the test dataset is smaller than that of the training dataset, which is a quite common phenomenon and has also been reported in other studies[26,27]. The RMSE values achieved are considered satisfactory for an MLP[18]. The force RMSE is typically low when the training set is simple[28–30]. However, it increases as the complexity of the training dataset grows, for example, when interfacial structures are involved[27,31,32]. This phenomenon is particularly evident in more general MLPs, as these potential functions need to cover a diverse range of atomic environments[33]. Therefore, the force RMSE obtained in this work remains within an acceptable range, sufficient to ensure the reliability of subsequent thermal transport property predictions. The predicted energies, forces, and virial stresses show excellent agreement with DFT reference values, as they are tightly clustered along the diagonal line. Moreover, the error distributions show that the majority of energy, force, and virial stress predictions deviate only slightly from DFT reference values. The distributions are sharply peaked at zero and symmetric, with minimal outliers, indicating high precision and reliability. The combination of RMSEs and favorable error distributions demonstrates the high accuracy and robustness of the trained NEP.

To evaluate the ability of NEP to describe crystal structures, the radial distribution functions (RDFs) calculated from DFT and NEP are compared, as shown in Fig. 3i. The peak positions and relative intensities predicted by NEP agree closely with the DFT results, indicating that the trained NEP achieves accuracy comparable to DFT in describing crystal structures. Beyond crystal structure, the accuracy of NEP in describing thermal properties is also crucial for this study. Phonon dispersion, a key thermal metric used to evaluate the quality of interatomic potentials, is frequently employed to validate MLP reliability. Figure 3a–d compares the phonon dispersion curves of β-Ga_2O_3, diamond, 4H-SiC, and Si computed using both DFT and NEP, demonstrating excellent agreement between NEP

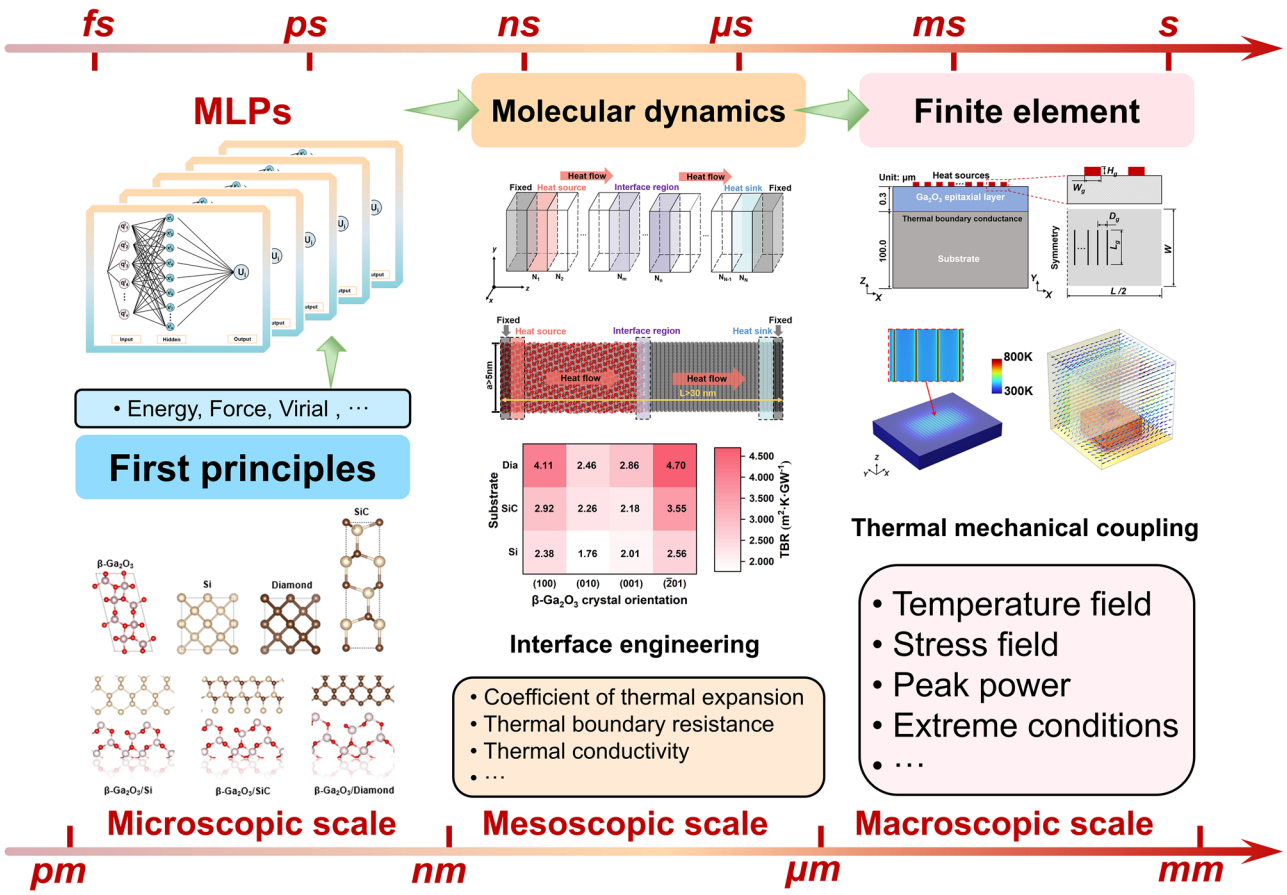

Fig. 1 | A multiscale simulation framework with cross-scale parameter transfer, spanning the microscopic, mesoscopic, and macroscopic scales, exemplified by β-Ga_2O_3-based heterostructures. A dataset constructed from first-principles calculations is used to train a high-accuracy machine learning interatomic potential via machine learning methods. Molecular dynamics simulations employing this potential can produce thermodynamic property parameters at the mesoscale with accuracy comparable to that of first-principles calculations. These parameters are then incorporated as inputs into a finite element model to perform macroscale thermo-mechanical coupling analyses, enabling efficient and accurate prediction of macroscopic thermodynamic properties of the material.

predictions and DFT results. The primitive cell models used for calculating the phonon dispersions of β-Ga_2O_3, diamond, 4H-SiC, and Si are shown in Fig. 3e-h. Finally, the thermal conductivities of diamond, Si, 4H-SiC, and β-Ga_2O_3 at 300 K predicted by the NEP method are compared with the values reported in the literature, as shown in Fig. 3j. It can be observed that the thermal conductivity predicted using NEP agrees well with the values reported in the literature[34–40]. In summary, the excellent agreement of the NEP-predicted RDFs and phonon dispersions with DFT reference calculations, together with the good match between NEP-predicted thermal conductivities and reported values, demonstrates that the developed NEP has great potential for atomistic simulations of interfacial thermal transport.

Mesoscopic-scale simulation of interfacial thermal transport and mechanism analysis

The simulation of interfacial thermal transport often requires system sizes on the order of tens to hundreds of nanometers, falling within the mesoscopic regime, as depicted in Fig. 4a. MD simulations are widely employed at this scale, as they can resolve atomic-level mechanisms while accessing length scales beyond those typical of DFT methods. In this study, non-equilibrium MD (NEMD) is utilized to investigate interfacial thermal transport. In this simulation, Si, SiC, and diamond layers are used as heat dissipation layers; thus, their ends are designated as heat sinks. In contrast, the end of the β-Ga_2O_3 layer is set as the heat source. To thoroughly investigate heat flux transport, the intermediate region is uniformly divided into multiple regions, as shown in Fig. 4a, b. Figure 4c shows the temperature distribution along the z-axis for 12 heterostructures with different interface configurations under NEMD simulations. The heat sink and heat source thermostats are maintained at 275 K and 325 K, respectively. The interfacial temperature jump is minimized when Si serves as the heat sink substrate, intermediate for SiC, and largest for diamond, indicating progressively higher interfacial thermal resistance in the latter cases. The interfacial TBR of the 12 interface configurations at 300 K is shown in Fig. 4d, e. Under the same heat sink material, interfaces formed with β-Ga_2O_3 (010) and (001) orientations exhibit lower TBR, while those based on (100) and ($\bar{2}$01) orientations show higher TBR. This behavior is likely attributed to the anisotropic intrinsic thermal conductivity of β-Ga_2O_3: the (010) and (001) orientations possess higher thermal conductivity, enabling efficient heat transport and reducing TBR; in contrast, the lower thermal conductivity along the (100) and ($\bar{2}$01) directions impedes heat flow, resulting in increased TBR. However, for identical β-Ga_2O_3 crystal orientations, the lowest TBR is observed when Si is used as the heat dissipation substrate, with higher values for SiC, and the highest TBR occurs with diamond. This observation contradicts conventional expectations, as diamond possesses an exceptionally high thermal conductivity, and SiC has a significantly higher thermal conductivity than Si. A temperature dependence of the TBR is also observed, with TBR decreasing as temperature increases for identical interface structures. This observation is also inconsistent with the conventional thermal transport behavior of bulk crystal materials. In bulk crystal materials, thermal conductivity typically decreases with increasing temperature, leading to degraded heat transfer performance. However, in heterostructure systems, the TBR decreases with rising temperature, which facilitates cross-interface heat transport. This opposite trend suggests that there may exist special phonon coupling mechanisms at the interface, warranting further investigation, particularly regarding its implications for

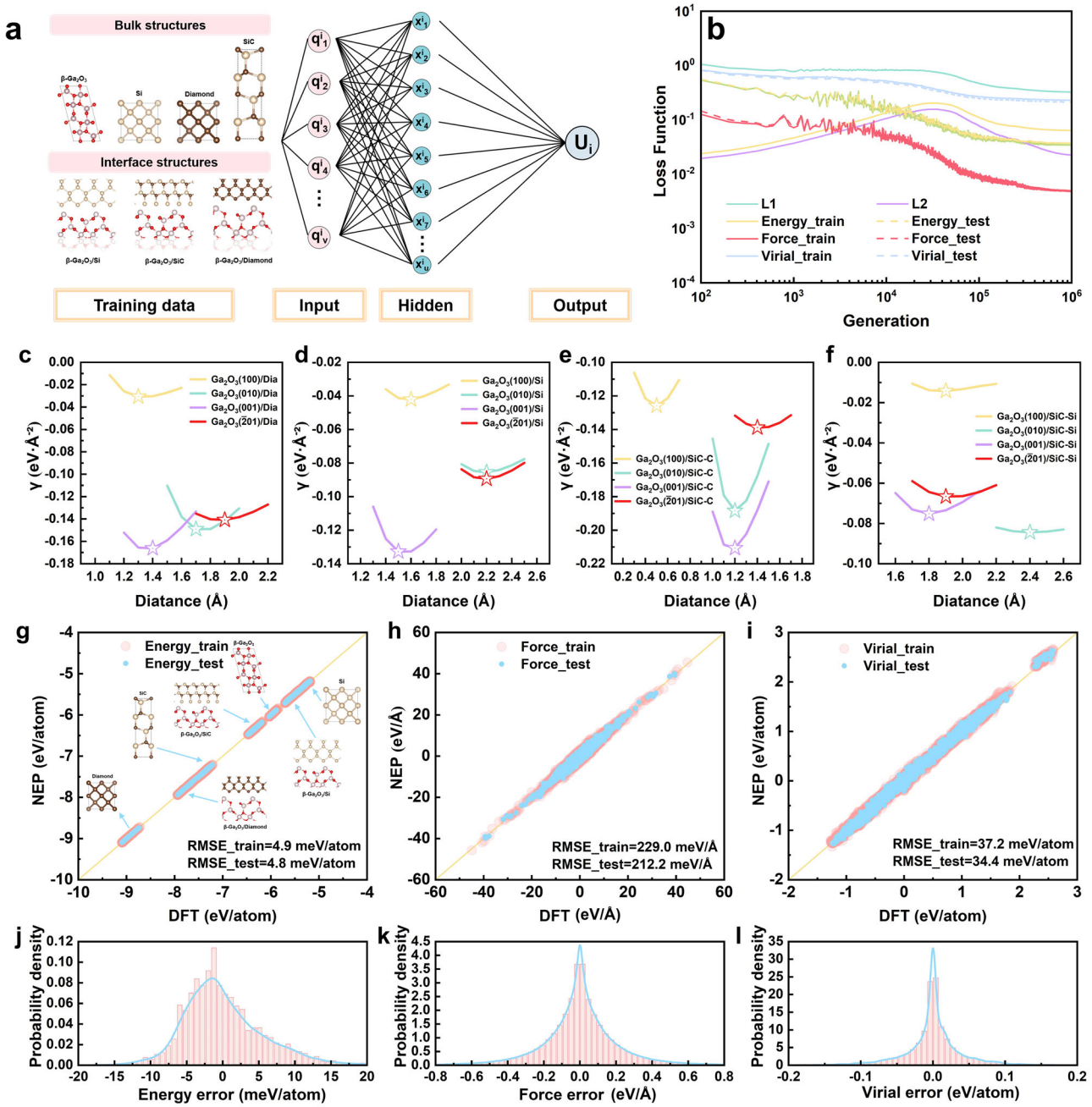

Fig. 2 | Schematic illustration of the NEP framework and machine learning performance. a Composition of the training dataset and schematic of the NEP model architecture. **b** Evolution of the loss function during the training iterations. **c–f** Interfacial energy as a function of interfacial distance for different interface structures. **g–i** Comparison between NEP-predicted and DFT-calculated energies, forces, and virial stresses. **j–l** Probability density distributions of the prediction errors for energy, forces, and virial stresses.

thermal management in macroscopic FE simulations. Figure 4f–h presents the TBR values of the 12 interface configurations over the temperature range from 200 K to 500 K. To obtain TBR values over the temperature range from 200 to 500 K, four sets of NEMD simulations were carried out, with heat sink and source thermostats set at (175 K/225 K), (275 K/325 K), (375 K/425 K), and (475 K/525 K), respectively.

To gain deeper insight into the underlying mechanism of the TBR variation trend, the VDOS of different single crystals at various temperatures, the contribution of phonon modes at different frequencies to interfacial thermal conductance (ITC), and the trend of cumulative ITC with phonon mode frequency are calculated, as shown in Fig. 5 and Fig. 6. As shown in Fig. 5a–c, the VDOS of β-Ga_2O_3 and the three substrate materials are compared. The highest VDOS overlap ratio is observed for β-Ga_2O_3 and Si (61.65%), followed by SiC (50.03%), with the lowest value corresponding to diamond (21.58%). This is also confirmed by the vibrational spectra of the heterostructures, as shown in Fig. 5e–g. There is a high degree of overlap in the vibrational spectra between Ga_2O_3 and Si, as well as between Ga_2O_3 and SiC, whereas a significant mismatch is observed between Ga_2O_3 and diamond. This may be one of the main underlying reasons for the lowest TBR at the β-Ga_2O_3/Si interface and the highest TBR at the β-Ga_2O_3/diamond interface, as a higher overlap of VDOS is more favorable for elastic phonon scattering at the interface. The VDOS of the four major crystal orientations of β-Ga_2O_3 is calculated to further analyze the influence of crystal orientation on TBR, as shown in Fig. 5d. β-Ga_2O_3 exhibits pronounced anisotropy, resulting in significant differences in the VDOS among its four crystal orientations. As can be seen from Fig. 5d, the (010) and (001) orientations

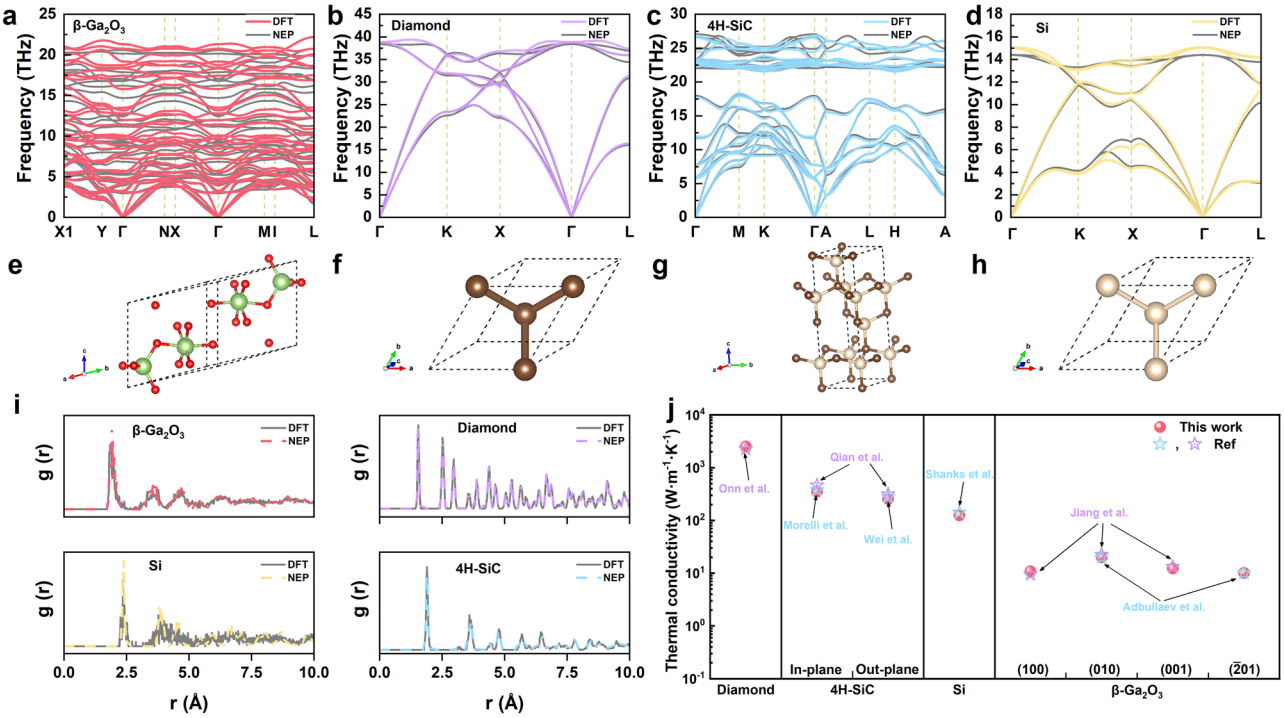

Fig. 3 | Assessment of the accuracy of the NEP in describing crystal structures and thermal properties. a–d Comparison of phonon dispersion curves for β-Ga_2O_3, diamond, 4H-SiC, and Si obtained from NEP and DFT calculations. **e–h** Primitive cell models used for calculating the phonon dispersions of β-Ga_2O_3, diamond, 4H-SiC, and Si. **i** Comparison of RDFs for β-Ga_2O_3, diamond, 4H-SiC, and Si computed using NEP and DFT. **j** Comparison of thermal conductivities of diamond, Si, 4H-SiC, and β-Ga_2O_3 predicted using the NEP with reference values.

have higher weight in the high-frequency range compared to the (100) and ($\bar{2}$01) orientations. This may be another fundamental reason why interfaces based on the β-Ga_2O_3 (010) and (001) orientations exhibit lower TBR, while those based on the (100) and ($\bar{2}$01) orientations exhibit higher TBR, under identical heat sink conditions.

The ICMA method facilitates a deeper understanding of the contribution of phonon modes at different frequencies to ITC[41,42]. The contribution of phonon modes at different frequencies to ITC for the 12 interface structures is shown in Fig. 6a–d. All phonon mode contributions to ITC have been normalized to facilitate comparison. It can be seen that phonon modes in the 0–10 THz frequency range make the dominant contribution to ITC, and the ITC of β-Ga_2O_3/Si interfaces is primarily contributed by phonons within this frequency range. Although the ITC of the β-Ga_2O_3/SiC interface is also contributed by phonon modes in the 0–10 THz range, the peak positions within this range are clearly shifted toward higher frequencies. Phonon modes in the 10–20 THz frequency range also make a non-negligible contribution to the β-Ga_2O_3/SiC interface. In addition to the contribution of medium and low frequency phonon modes in the range of 0–20 THz, high frequency phonon modes in the range of 25–40 THz also play an important role in the ITC of β-Ga_2O_3/diamond interface. This frequency range exceeds the intrinsic phonon frequency range of β-Ga_2O_3, indicating that the phonon modes in this region are primarily derived from diamond or may involve contributions from inelastic phonon scattering. This may be another fundamental reason why the TBR of the β-Ga_2O_3/diamond interface is significantly higher than that of the β-Ga_2O_3/Si and β-Ga_2O_3/SiC interfaces. Figure 6e–h show the trend of cumulative ITC as a function of phonon mode frequency for the 12 interface structures. To enable direct comparison, all cumulative ITC curves have been normalized. It can be observed that the ITC of the β-Ga_2O_3/Si and β-Ga_2O_3/SiC interfaces reaches its maximum value before the phonon mode frequency reaches 22.5 THz, within the intrinsic phonon mode frequency range of β-Ga_2O_3. In contrast, the ITC of the β-Ga_2O_3/diamond interface reaches its maximum after the phonon mode frequency exceeds 25 THz, beyond the intrinsic phonon frequency range of β-Ga_2O_3. This observation is consistent with the above analysis of phonon mode contributions to ITC and may also be one of the key factors influencing the TBR. Furthermore, to gain deeper insight into the underlying mechanism of the temperature dependence of TBR, the intrinsic VDOS of β-Ga_2O_3, Si, SiC, and diamond at different temperatures is calculated, as shown in Fig. 7a–c. A further observation reveals that the intrinsic VDOS of β-Ga_2O_3, Si, SiC, and diamond shifts with rising temperature, as highlighted in the magnified views within the red boxes. The overlap between the VDOS of β-Ga_2O_3 and that of Si, SiC, and diamond gradually increases as temperature rises, as shown in the insets of Fig. 7a–c. This may be one of the primary reasons for the decrease in TBR with increasing temperature. The PPR at the interface region at different temperatures is shown in Fig. 7d, e. It is evident that with the increase of temperature, the phonon modes at the β-Ga_2O_3/Si and β-Ga_2O_3/SiC interfaces in the 10–20 THz frequency range, as well as the phonon modes at the β-Ga_2O_3/diamond interface in the 10–30 THz range, show a significant enhancement in their PPR. This may be another major reason why the TBR decreases as the temperature increases.

In summary, this part employs mesoscale MD simulations to systematically predict the TBR of 12 interface structures across the β-Ga_2O_3/Si, β-Ga_2O_3/SiC, and β-Ga_2O_3/diamond systems under varying temperatures. Furthermore, by combining VDOS and PPR analysis with the ICMA method, the underlying mechanisms responsible for the differences in TBR are elucidated from a combined micro- to mesoscale perspective. The predicted results show that the TBR of the β-Ga_2O_3/diamond interface is significantly higher than that of the β-Ga_2O_3/Si and β-Ga_2O_3/SiC interfaces, which contradicts the conventional assumption that high-thermal-conductivity materials are inherently favorable for heat dissipation. This is because the thermal performance of heterostructures depends not only on the bulk thermal conductivity of the heat

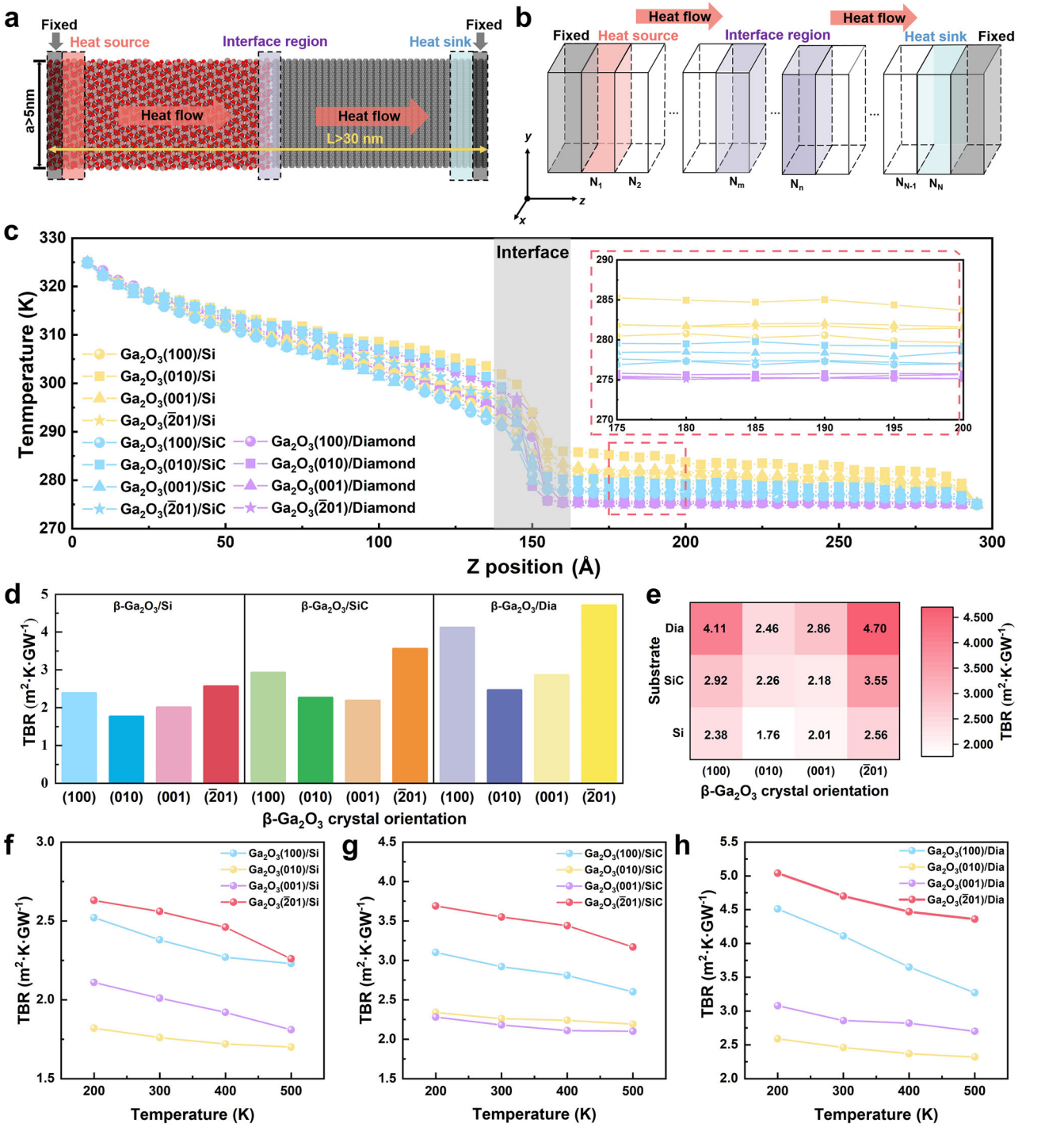

Fig. 4 | Simulation results of β-Ga_2O_3/substrate heterostructures and TBR predictions under different conditions. a Schematic illustration of the β-Ga_2O_3-based heterostructure model. **b** Schematic of the region composition in the NEMD simulation. **c** Temperature distribution along the z-axis for the 12 interface configurations. **d**,**e** TBR values of the 12 interface configurations at 300 K. **f**–**h** TBR values of the 12 interface configurations over the temperature range from 200 to 500 K.

sink, but also critically on the TBR. It is also found that the TBR of the same interface structure is not constant, but decreases with increasing temperature, contrary to the assumption in previous studies that TBR remains invariant[43–45]. This indicates that interfacial heat transfer becomes more complex in practical device applications, where temperature dependence must be taken into account. The coupling of these complex processes to determine the final heat dissipation effect of the device is difficult to achieve in mesoscopic simulation. Therefore, further research at the macroscopic scale is needed.

Macroscopic-scale simulation of thermo-mechanical coupling and performance prediction

FE simulations are conducted based on the TBR values obtained from MD simulations to investigate the macroscopic manifestation of mesoscale coupled processes. Further information on the TBR fitting function can be found in the methods section. A macroscale FE model is developed, as shown in Fig. 8a. The β-Ga_2O_3-based heterostructure device consists of an epitaxial β-Ga_2O_3 layer, a heat-dissipating substrate layer, and the interfacial region between them, with the heat source positioned on the top

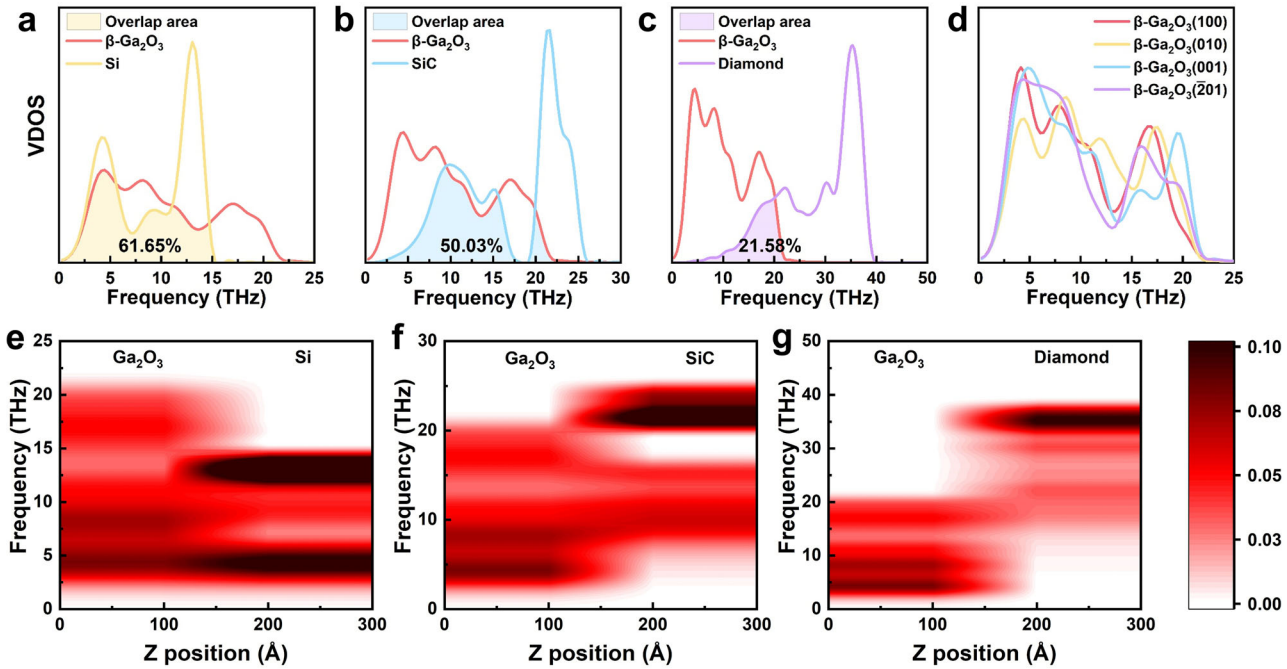

Fig. 5 | Vibrational density of states and vibrational spectra of β-Ga_2O_3-based heterostructures. a VDOS and overlap ratio between β-Ga_2O_3 and Si. **b** VDOS and overlap ratio between β-Ga_2O_3 and SiC. **c** VDOS and overlap ratio between β-Ga_2O_3 and diamond. **d** VDOS of β-Ga_2O_3 along different crystal orientations. **e** Vibration spectra of β-Ga_2O_3/Si heterostructures. **f** Vibration spectra of β-Ga_2O_3/SiC heterostructures. **g** Vibration spectra of β-Ga_2O_3/diamond heterostructures.

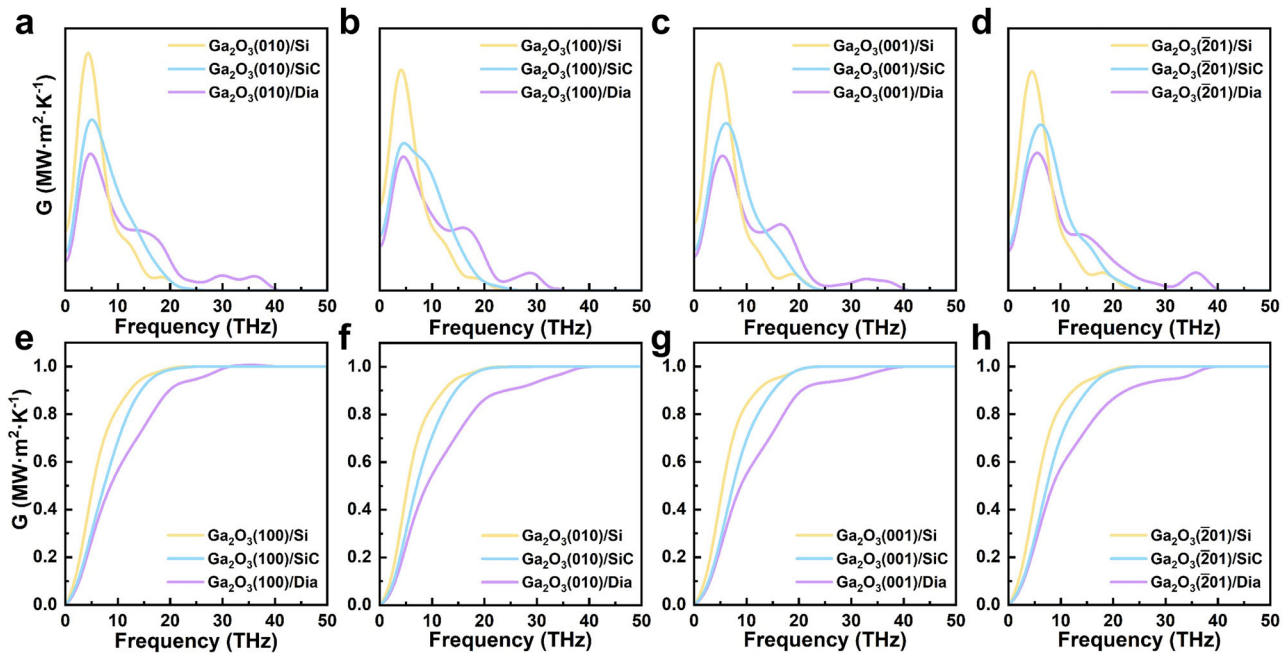

Fig. 6 | Interfacial thermal conductance modal analyses. a–d Contribution of phonon modes at different frequencies to ITC in 12 interface structures. **e–h** Cumulative ITC as a function of phonon mode frequency in 12 interface structures.

surface of the β-Ga_2O_3 layer. As shown in Fig. 8b, a non-uniform meshing strategy is adopted, in which a minimum element size of 200 nm is employed near each gate finger structure to accurately resolve the steep temperature gradients in the vicinity of the heat source. Figure 8c presents the steady-state temperature field of the device obtained from FE simulations under power loading conditions. As shown in Fig. 8d–g, the temperature distribution on the β-Ga_2O_3 surface is non-uniform, with the maximum temperature rise occurring beneath the gate region. Additionally, it can be observed that under the same load power and β-Ga_2O_3 crystal orientation, the peak temperature is lowest when diamond is used as the thermal substrate, followed by SiC, and highest with Si as the thermal substrate. The observed trend is primarily attributed to the thermal conductivity of the substrate: higher substrate thermal conductivity leads to lower peak temperatures and improved heat dissipation. This indicates that, in macroscopic device applications, thermal conductivity remains the dominant factor governing the cooling performance

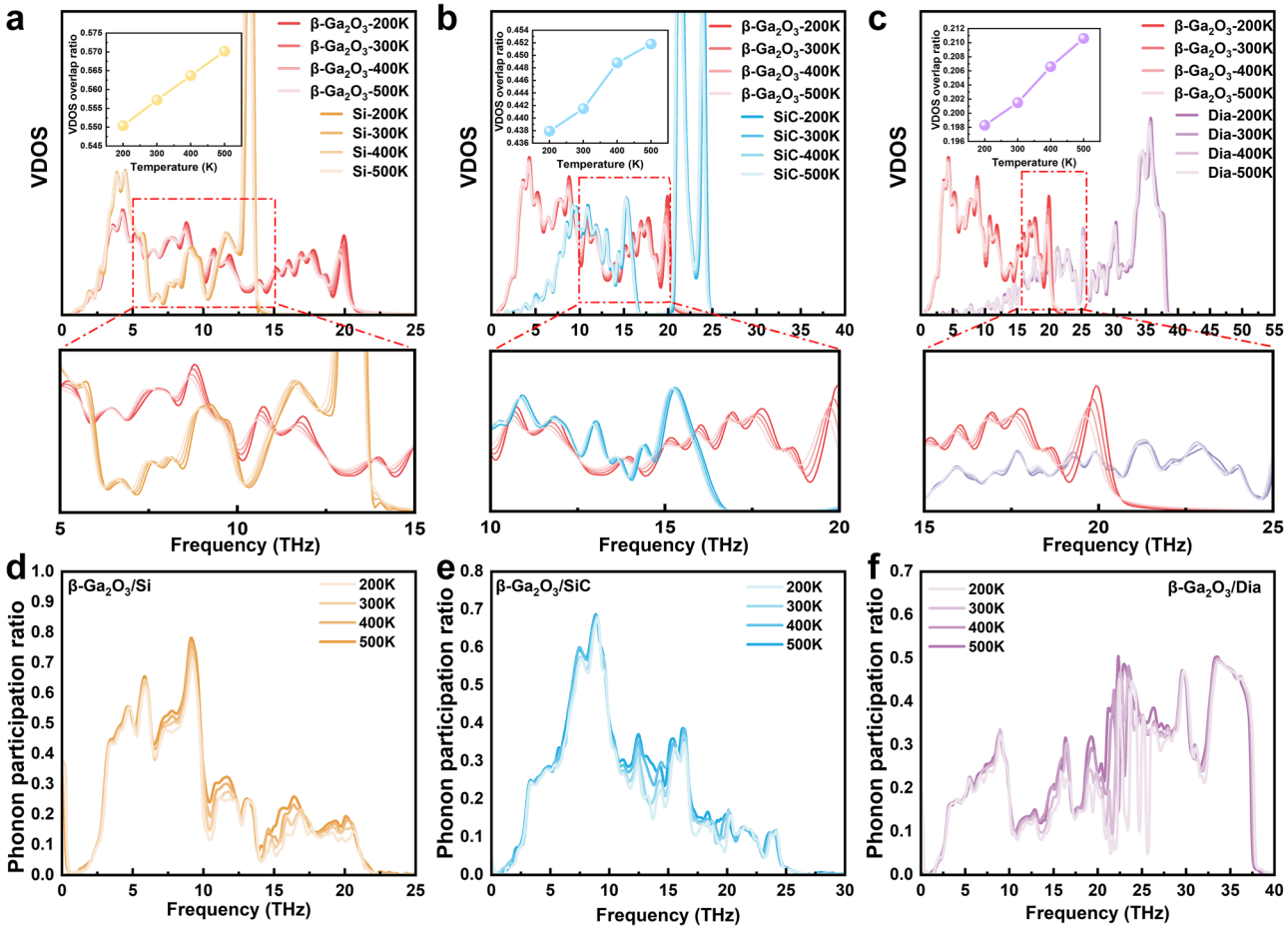

Fig. 7 | Vibrational density of states and phonon participation ratio of β-Ga_2O_3-based heterostructures. **a** VDOS and overlap ratio between β-Ga_2O_3 and Si at different temperatures. **b** VDOS and overlap ratio between β-Ga_2O_3 and SiC at different temperatures. **c** VDOS and overlap ratio between β-Ga_2O_3 and diamond at different temperatures. **d** PPR at β-Ga_2O_3/Si interface region at different temperatures. **e** PPR at β-Ga_2O_3/SiC interface region at different temperatures. **f** PPR at β-Ga_2O_3/diamond interface region at different temperatures.

of heterostructures. It is also observed that, with the same heat-dissipating substrate, different crystal orientations of β-Ga_2O_3 result in distinct peak temperatures. The lower peak temperature observed in devices with β-Ga_2O_3 oriented along the (010) direction can be attributed to two factors: the higher thermal conductivity of β-Ga_2O_3 in (010) orientation and the relatively low TBR at the interface with the substrate.

Furthermore, 500 K is defined as the limit temperature for device damage, and the maximum allowable power is calculated for 12 different heterostructures, as shown in Fig. 8h. When Si is used as the heat-dissipating substrate, the maximum power density is approximately 10 W/mm; for SiC, it ranges from 16 to 20 W/mm; and for diamond, it increases to 18–26 W/mm. Notably, the β-Ga_2O_3 (010)/diamond heterostructure achieves a maximum power density of 26 W/mm, reaching approximately 226% of the value achieved with the Si-based device. It is also observed that the influence of β-Ga_2O_3 crystal orientation on the maximum power density is negligible when the substrate has low thermal conductivity. However, as the substrate thermal conductivity increases, the orientation dependence becomes significant. Particularly with diamond substrates, the difference in maximum power density between orientations reaches up to 8 W/mm, corresponding to a ~ 44% increase. To elucidate the origin of this behavior, the temperature rise across different regions of the heterostructure is decomposed. As shown in Fig. 8i, the contribution of each layer to the total junction-to-sink temperature difference is quantified at varying power levels. Taking the β-Ga_2O_3 (100) orientation as an example, as the substrate thermal conductivity increases, the contribution of the substrate region to the total temperature rise decreases significantly, while the contribution of the β-Ga_2O_3 layer increases notably, along with a moderate rise in the interfacial contribution. Under higher power loads, the relative contributions from the substrate and β-Ga_2O_3 layer in Si- and SiC-substrate heterostructures exhibit significant changes, whereas the interfacial contribution remains nearly unchanged. In contrast, for diamond-substrate devices, the variations in the substrate and β-Ga_2O_3 layer contributions are much smaller, but the interfacial component shows a significant change, indicating that interface optimization becomes the key bottleneck for further improving thermal performance. Therefore, reducing the interfacial TBR represents a critical challenge for optimizing the thermal management of β-Ga_2O_3/diamond-based devices.

To further investigate the influence of interface structure on thermal-mechanical performance, thermomechanical coupling simulations on heterostructure devices with 12 different interface designs are conducted. The lateral von Mises stress distributions at the β-Ga_2O_3 layer and the substrate layer are shown in Fig. 8j–m. Under identical β-Ga_2O_3 orientations, the von Mises stress is highest for Si substrates, followed by SiC, and lowest for diamond. This trend is primarily attributed to thermal stress. Because the Si substrate has the lowest thermal conductivity, the surface of the β-Ga_2O_3 layer heats up the most during device operation, leading to higher thermal stress. In contrast, the diamond substrate has very high thermal conductivity, which helps dissipate heat quickly, lowering the operating temperature and reducing thermal stress buildup. Under identical substrates, the β-Ga_2O_3 (010) orientation exhibits the lowest surface temperature but the highest von Mises stress. This is likely attributed to significant lattice mismatch and CTE mismatch between the β-Ga_2O_3 (010) interface and the substrate. Therefore, the crystal orientation of β-Ga_2O_3 is critical for

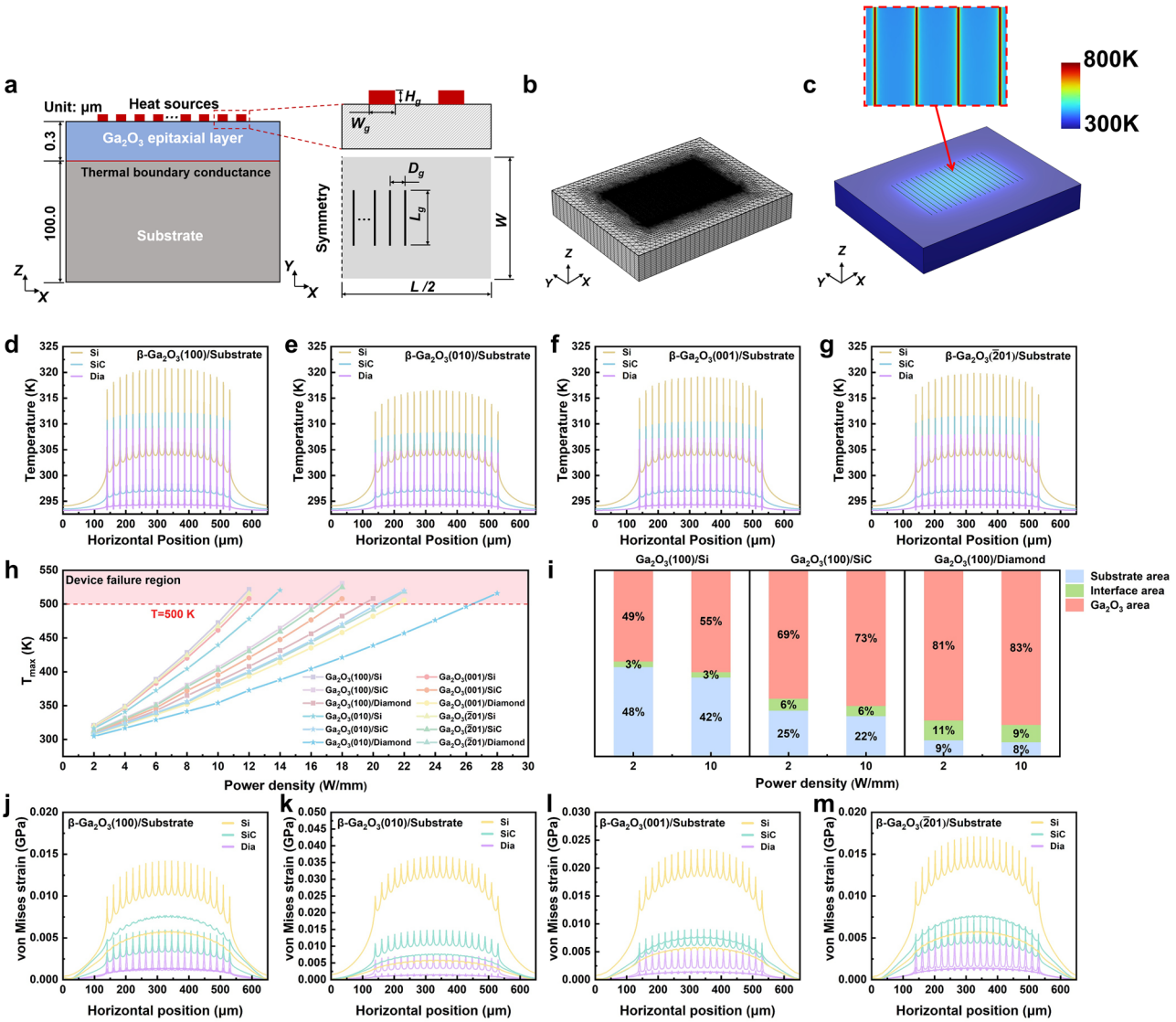

Fig. 8 | Schematic diagram and results of macroscale FE simulation. a Schematic cross-sectional view of the β-Ga_2O_3 device stack and the location of the heat source. **b** Details of the representative FE mesh used in the simulations. **c** Simulated steady-state temperature distribution of the device. **d–g** Surface lateral temperature profiles of the 12 heterostructures under a power density of 2 W/mm. **h** Maximum surface temperature of the 12 heterostructures at varying input power levels. **i** Contribution of the β-Ga_2O_3 layer, interfacial layer, and substrate layer to the total temperature rise under different power densities. **j–m** Lateral von Mises stress distributions in the β-Ga_2O_3 and substrate layers of the 12 heterostructures under a power density of 2 W/mm.

β-Ga_2O_3-based heterostructures, as it not only influences thermal dissipation but also significantly affects interfacial thermal stress. Achieving high heat dissipation while minimizing interfacial stress is also a key challenge in optimizing β-Ga_2O_3-based heterostructures.

In summary, this part conducts macroscopic FE simulations based on the interfacial TBR values obtained from mesoscale MD simulations, aiming to systematically investigate the macroscopic thermal response induced by interfacial behaviors at the mesoscale. The analysis reveals that the intrinsic thermal conductivity of the heat-dissipating substrate remains the dominant factor governing the thermal performance of the heterostructure. However, when the heat-dissipating substrate possesses high thermal conductivity, the influence of interfacial TBR on the overall thermal performance becomes significantly more pronounced with increasing operating temperature. Under such conditions, the thermal bottleneck shifts from the bulk substrate to the interface region, highlighting the growing importance of interface engineering in advanced heterostructures. Furthermore, coupled thermomechanical analysis demonstrates that the crystal orientation of β-Ga_2O_3 plays a critical role in β-Ga_2O_3-based heterostructures, as it not only substantially affects the system's heat dissipation capability but also profoundly influences the distribution of interfacial thermal stress. This trade-off between thermal efficiency and mechanical reliability represents a key challenge in the design of β-Ga_2O_3-based devices. Therefore, further optimization of interfacial thermal transport and effective thermal stress management are essential to fully unlock the potential of β-Ga_2O_3-based high-power electronic devices.

Discussion

In this work, an NEP is developed based on a training dataset generated from first-principles calculations at the atomic scale, aiming to simulate interfacial heat transfer in β-Ga_2O_3/substrate heterostructures with substrates including Si, SiC, and diamond. This NEP enables an efficient and accurate mapping of atomic-scale physical quantities (such as atomic energies and forces) for use in mesoscale MD simulations, thereby achieving MD accuracy comparable to that of the DFT method. Subsequently, the mesoscale thermal transport parameters obtained from MD simulations are used as input for macroscopic FE simulations. These parameters include the TBR at various interfaces and temperatures and the temperature-dependent thermal conductivity of β-Ga_2O_3 along different crystal orientations, both of

which are rarely reported in the literature. The MD method within this multiscale framework effectively overcomes the problems of excessive computational cost in first-principles calculations and insufficient accuracy in traditional MD, enabling FE simulations conducted within this framework to obtain simulation results that are relatively close to real physical values, even in the absence of experimental data. This work establishes a multiscale thermal transport framework spanning from the atomic and mesoscale to the macroscale, enabling comprehensive cross-scale thermal analysis.

First, the accuracy of the NEP is validated at the atomic scale by comparing the predicted phonon dispersion relations and RDFs with those obtained from the DFT method. Building upon this, interfacial TBR for 12 interface configurations is subsequently predicted across a range of temperatures using the NEP within mesoscale MD simulations. The prediction results reveal that the TBR at the β-Ga_2O_3/diamond interface is significantly higher than that at the β-Ga_2O_3/Si and β-Ga_2O_3/SiC interfaces, which contradicts the conventional assumption that high-thermal-conductivity materials inherently facilitate superior heat dissipation. Furthermore, the study shows that the TBR for a specific interface structure is not constant, but rather decreases with increasing temperature. This trend contradicts the common assumption of a constant TBR in previous studies. By combining VDOS, PPR analysis with the ICMA method, the underlying mechanisms for the differences in TBR are elucidated from an integrated perspective spanning the atomic to mesoscale. The heat dissipation performance of heterostructures depends not only on the thermal conductivity of the heat sink, but also on the TBR. Therefore, these findings reveal the complexity of interfacial heat transfer under practical device operating conditions and highlight the necessity of accounting for the temperature dependence of TBR in high-fidelity thermal management design. Finally, macroscopic FE simulations are performed using the interfacial TBR values obtained from mesoscale MD simulations, aiming to systematically investigate the macroscopic thermal response induced by interfacial phenomena at the mesoscale. The analysis reveals that the thermal conductivity of the heat-dissipating substrate remains the dominant factor governing the thermal performance of the heterostructure. However, when the heat-dissipating substrate exhibits high thermal conductivity, the influence of TBR on the overall thermal performance becomes increasingly pronounced with rising operating temperature. Under such conditions, the thermal bottleneck shifts from the bulk substrate to the interface region, highlighting the growing importance of interface engineering in advanced heterostructures. Furthermore, coupled thermomechanical analysis demonstrates that the crystal orientation of β-Ga_2O_3 plays a critical role in β-Ga_2O_3-based heterostructures, as it not only significantly affects the system's heat dissipation capability but also profoundly influences the distribution of interfacial thermal stress. This trade-off between heat dissipation efficiency and mechanical reliability represents a key challenge in the design of β-Ga_2O_3-based devices. Therefore, further optimization of interfacial thermal transport and effective management of thermal stress are essential to fully unlock the performance potential of β-Ga_2O_3-based high-power electronic devices. This study not only provides valuable optimization strategies for thermal management in β-Ga_2O_3-based systems, but also lays the foundation for multiscale investigations of thermal management in other materials.

Methods

Details of training dataset and NEP

The 2400 structures used for the training dataset consist of bulk and interface configurations. All of these structures were generated through ab initio MD (AIMD) simulations performed with the Vienna Ab initio Simulation Package (VASP). The simulations employed the projector augmented wave method and the Perdew-Burke-Ernzerhof exchange-correlation functional[46–49]. A cutoff of 700 eV was applied in all structures. For the bulk configurations (β-Ga_2O_3, diamond, Si, and 4H-SiC), the initial configurations included the pristine fully relaxed cells as well as configurations generated by applying small atomic displacements and appropriate strains to those relaxed geometries. All these initial structures, including the unperturbed pristine cells, were subjected to AIMD simulations, producing 1500 trajectory frames per material (6000 frames in total). To avoid strong temporal correlations, every 10th frame was subsampled, resulting in 150 frames per material (600 frames in total) for the training dataset. An additional 75 frames per material (300 frames in total) were randomly selected for the test dataset. For the interface configurations (β-Ga_2O_3/diamond, β-Ga_2O_3/4H-SiC, and β-Ga_2O_3/Si), interfaces with various crystal orientations were constructed. The fully relaxed pristine interfaces as well as configurations subjected to small atomic displacements and appropriate strains were included. Each interface configuration was subjected to an AIMD simulation, generating 3600 trajectory frames per system (10,800 frames in total across all three systems). To reduce strong temporal correlations, every 18th frame was subsampled, producing 600 frames per interface configuration (1800 in total) for the training dataset, and 300 frames per system (900 in total) were randomly selected for the test dataset. In total, the training dataset comprises 600 bulk and 1800 interface configurations, amounting to 2400 configurations, while the test dataset comprises 300 bulk and 900 interface configurations, totaling 1200 configurations. All these structures were derived from physically meaningful AIMD trajectories that span a broad range of atomic environments, temperatures, and mechanical deformations. This strategy ensures sufficient diversity and representativeness of the training data while maintaining high fidelity through first-principles accuracy.

To more clearly illustrate the composition of the training and test datasets and the temperature distribution of the training set, Fig. 9 is provided. As shown in Fig. 9, the training and test datasets are identical in terms of structural composition and the proportion of each structure type. Both datasets include four bulk configurations (β-Ga_2O_3, diamond, Si, and 4H-SiC) and three interface configurations (β-Ga_2O_3/diamond, β-Ga_2O_3/4H-SiC, and β-Ga_2O_3/Si). In each dataset, each bulk configuration accounts for 6.25% of the total, while each interface configuration accounts for 25%. The temperature distribution of the 2400 configurations in the training dataset is shown in Fig. 9b. The number of configurations within each 100 K temperature interval was counted. During the AIMD simulations, the system temperature was set to range from 10 K to 1000 K, and the number of configurations sampled in each temperature interval was not strictly controlled. Based on the results, the configurations are approximately uniformly distributed across the 10–1000 K range, with each interval containing more than 5% of the total configurations. Only a small number of configurations fall in the range of 1000–1100 K due to thermal fluctuations. Figure 9c–i shows the temperature distribution of each component in the training dataset. The number of configurations is relatively higher in certain temperature intervals. All temperature intervals within the 10–1000 K range contain more than 5% of the total configurations, except for the 1000–1100 K interval, which accounts for a significantly smaller fraction.

Structural models are constructed and processed using VASPKIT[50]. Visualization of the atomic configurations is performed using VESTA, OVITO and NepTrainKit[51–53]. Table 1 lists the hyperparameters employed in the NEP training. The model is implemented using NEP4, and the potential includes the elements Ga, O, C, and Si. The NEP is a neural network (NN) potential consisting of an input layer, hidden layers, and an output layer, as shown in Fig. 1a. It maps the descriptor vector q_v^i of the central atom i to its site energy Ui. The formula can be expressed as:

$$U_i = \sum_{\mu=1}^{N_{neu}} \omega_\mu^{(1)} tanh\left(\sum_{v=1}^{N_{des}} \omega_{\mu v}^{(0)} q_v^i - b_\mu^{(0)}\right) - b^{(1)} \quad (1)$$

The detailed information about the above formula and detailed definitions of the hyperparameters can be found in related works[18,54].

NEMD simulation

The NEMD method, derived from Fourier's law, is used to explore the heat transfer at the β-Ga_2O_3/ substrate interface in this work. The heat flux J_Q in

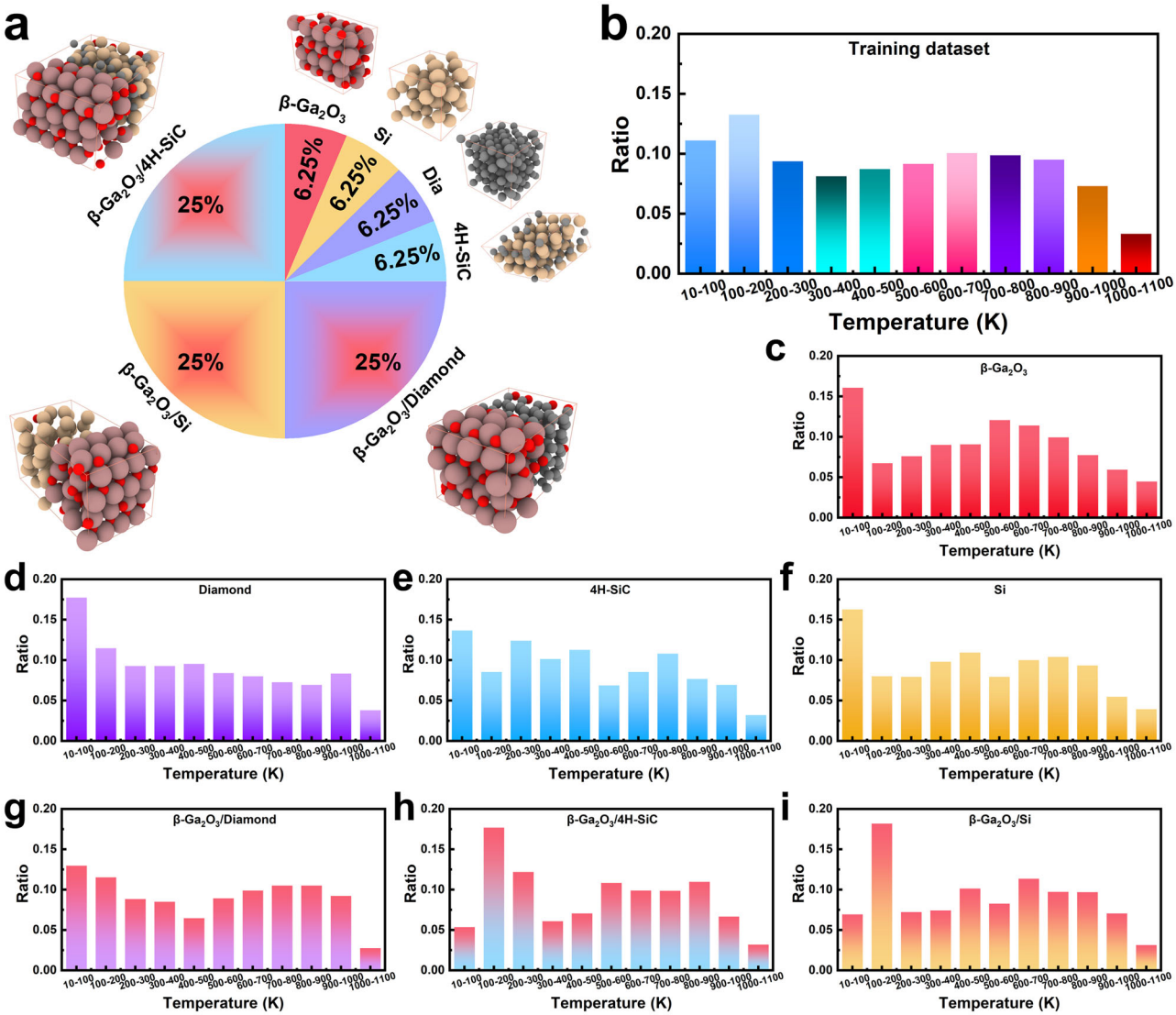

Fig. 9 | Composition of the training and test datasets and temperature distribution of the training dataset. a Composition of the training and test datasets. **b** Temperature distribution of the training dataset. **c-i** Temperature distribution of each component in the training dataset.

Table 1 | Hyperparameters for the NEP training

Parameter	Value	Parameter	Value
version	NEP4	type	4 Ga O C Si
r_C^R	6 Å	r_C^A	4 Å
$n_{\max}^R$	8	$n_{\max}^A$	8
N_{basis}^R	10	N_{basis}^A	10
$l_{\max}^{3b}$	4	$l_{\max}^{4b}$	2
$l_{\max}^{5b}$	0	N_{neuron}	60
N_{batch}	2400	$N_{generation}$	1,000,000

the β-Ga_2O_3/ substrate system is obtained as:

$$J_Q = \frac{|dQ/dt|}{A} \tag{2}$$

where $|dQ/dt|$ refers to the energy exchange rate, while A is the area of the simulation box that is perpendicular to the heat flux. Based on Fourier's law, TBR is defined as[55]:

$$\mathrm{TBR} = \frac{\Delta T}{J_Q} \tag{3}$$

where ΔT denotes the temperature difference across the interface region. VDOS is calculated using the Fourier transform of the atomic velocity autocorrelation function, as detailed below[56]:

$$VDOS(\omega) = \int_0^\infty e^{-2\pi i\omega t} \frac{<\sum_i v_i(t_0)\cdot v_i(t_0+t)>}{<\sum_i v_i(t_0)\cdot v_i(t_0)>} dt \tag{4}$$

where ω denotes the frequency, t_0 refers to the start time, t represents correlation time, and v_i represent the velocity vector of the i-th atom. The VDOS for different crystal orientations is the projected vibrational density of states along a specific crystal orientation. The PPR calculation can be conducted as follows[57]:

$$PPR(\omega) = \frac{1}{N}\frac{(\sum_i VDOS_i^2(\omega))^2}{\sum_i VDOS_i^4(\omega)} \tag{5}$$

Table 2 | Geometric parameters of β-Ga_2O_3-based device structures in FE simulations

Definition	Value
Length of structural (*L*)	670 μm
Width of structural (*W*)	530 μm
Heat source length (L_g)	240 μm
Heat source width (W_g)	0.5 μm
Heat source thickness (H_g)	0.2 μm
Gate-gate pitch spacing (D_g)	20 μm

Table 3 | Thermal conductivity parameters used in the FE simulation

Material	Thermal Conductivity ($W·m^{-1}·K^{-1}$)	Heat Capacity ($J·kg^{-1}·K^{-1}$)	Mass Density ($kg·m^{-3}$)
β-Ga_2O_3	β-Ga_2O_3(100):$10.85\times(T/300)^{-1.2611}$ β-Ga_2O_3(010):$20.07\times(T/300)^{-1.4336}$ β-Ga_2O_3(001):$13.18\times(T/300)^{-1.2966}$ β-Ga_2O_3($\bar{2}$01):$10.13\times(T/300)^{-1.3770}$	100	5940
Si	$150\times(T/300)^{-1.3}$	700	2329
SiC	$420\times(T/300)^{-1.3}$	650	3210
SCD	in plane:$1185\times(T/300)^{-0.55}$ through plane:$1480\times(T/300)^{-0.55}$	516	3515

Prior to heat transfer analysis, the system underwent full structural relaxation under the NPT ensemble. Temperature control was maintained using the NVT ensemble with thermostats. To induce a thermal gradient, Langevin thermostats were applied to designated source and sink regions at opposite ends of the structure for a duration of 0.5 ns, initiating steady heat conduction. Following this, the temperature profile along the heat transport direction was recorded over a 2 ns production run. Data were sampled every 50 ps, and every 50 consecutive data points were averaged. This entire simulation protocol was repeated 80 times, and the final temperature distribution was obtained by averaging the results across all runs. To simulate realistic operating conditions, heat was introduced on the β-Ga_2O_3 side and extracted from the heat-dissipation substrate side, establishing a heat flux directed from β-Ga_2O_3 to the substrate. After initial relaxation, atoms in the terminal regions along the *z*-axis were held fixed, while periodic boundary conditions were applied in the lateral directions (*x* and *y*). All models used in this study have dimensions exceeding 5 nm × 5 nm × 30 nm, with minor variations depending on specific interface configurations.

FE simulation

The specific geometric parameters of the β-Ga_2O_3-based device structure in the FE simulations are shown in Fig. 8a and Table 2. Approximately 1.3 million hexahedral and prismatic mesh elements were used in the FE simulations. A fine mesh with a minimum size of 200 nm was applied near each gate finger to accurately resolve the steep temperature gradients in the vicinity of the heat source, as illustrated in Fig. 8b. The bottom surface of the heat sink was set to 300 K, while all other boundaries were designated as adiabatic boundaries. The thermal properties of the materials used in the FE simulations are listed in Table 3. The thermal conductivities of β-Ga_2O_3 along four crystal orientations were derived from MD simulations and carefully validated against the limited experimental data available[38,39]. All other parameters, such as the thermal conductivities of diamond, Si, and SiC were directly taken from previously reported literature, as these values have been extensively validated by both experimental measurements and simulations[43,44,58]. The TBR in the FE simulations was modeled as a temperature-dependent function, obtained by fitting a curve to the TBR values from MD simulations for each of the 12 configurations, as shown in Table 4.

Table 4 | TBR parameters used in the FE simulations (200–500 K)

Interface type	TBR ($m^2·K·GW^{-1}$)
β-Ga_2O_3(100)/Si	$0.915997e^{-0.004581T}+2.153800$
β-Ga_2O_3(010)/Si	$0.676198e^{-0.005514T}+1.153350$
β-Ga_2O_3(001)/Si	$0.703946e^{-0.005568T}+1.820478$
β-Ga_2O_3($\bar{2}$01)/Si	$0.944754e^{-0.004795T}+1.725330$
β-Ga_2O_3(100)/SiC	$1.492900e^{-0.004568T}+2.517400$
β-Ga_2O_3(010)/SiC	$1.459900e^{-0.004592T}+2.516200$
β-Ga_2O_3(001)/SiC	$0.818977e^{-0.006734T}+2.067170$
β-Ga_2O_3($\bar{2}$01)/SiC	$1.436738e^{-0.003870T}+3.057320$
β-Ga_2O_3(100)/diamond	$3.776362e^{-0.004212T}+2.931413$
β-Ga_2O_3(010)/diamond	$1.039700e^{-0.005986T}+2.278600$
β-Ga_2O_3(001)/diamond	$1.326700e^{-0.005532T}+2.635000$
β-Ga_2O_3($\bar{2}$01)/diamond	$2.262100e^{-0.002547T}+3.669200$

Data availability

To ensure the reproducibility of the models developed in this study, all datasets will be made publicly available in an open-access repository: https://github.com/wugai-whu/NEP-Ga2O3-substrate-thermal-conductivity.git. The more specific explanation and help will be made available upon request.

Received: 17 November 2025; Accepted: 6 February 2026;
Published online: 18 February 2026

References

1. Li, M. et al. Electrically gated molecular thermal switch. *Science* **382**, 585–589 (2023).
2. Hao, M., Li, J., Park, S., Moura, S. & Dames, C. Efficient thermal management of Li-ion batteries with a passive interfacial thermal regulator based on a shape memory alloy. *Nat. Energy* **3**, 899–906 (2018).
3. Wu, K. et al. Mechanochemistry-mediated colloidal liquid metals for electronic device cooling at kilowatt levels. *Nat. Nanotechnol.* **20**, 104–111 (2025).
4. Kang, J. S. et al. Integration of boron arsenide cooling substrates into gallium nitride devices. *Nat. Electron.* **4**, 416–423 (2021).
5. Zacharias, M. et al. Efficient first-principles methodology for the calculation of the all-phonon inelastic scattering in solids. *Phys. Rev. Lett.* **127**, 207401 (2021).
6. Liu, F., Mao, R., Liu, Z., Du, J. & Gao, P. Probing phonon transport dynamics across an interface by electron microscopy. *Nature* **642**, 1–6 (2025).
7. Ao, C., Zhou, N., Xu, B. & Chen, Z. Micrometer-scale composite pin-fin diamond microchannel heat sink for near-10-kilowatt-level chip thermal management. *Energy* **333**, 137392 (2025).
8. Shi, H. et al. Investigation of heat dissipation and electrical properties of diamond interposer for 2.5-D packagings. *IEEE Trans. Compon. Packaging Manuf. Technol.* **14**, 1601–1609 (2024).
9. Song, C., Kim, J. & Cho, J. The effect of GaN epilayer thickness on the near-junction thermal resistance of GaN-on-diamond devices. *Int. J. Heat. Mass Transf.* **158**, 119992 (2020).
10. Hua, Y., Li, H. & Cao, B. Thermal spreading resistance in ballistic-diffusive regime for GaN HEMTs. *IEEE Trans. Electron Dev.* **66**, 3296–3301 (2019).

11. Deringer, V. L., Caro, M. A. & Csányi, G. Machine learning interatomic potentials as emerging tools for materials science. *Adv. Mater.* **31**, 1902765 (2019).
12. Xu, K. et al. NEP-MB-pol: a unified machine-learned framework for fast and accurate prediction of water's thermodynamic and transport properties. *npj Comput. Mater.* **11**, 279 (2025).
13. Sun, Z. et al. Heat transport exploration through the GaN/diamond interfaces using machine learning potential. *Int. J. Heat. Mass Transf.* **241**, 126724 (2025).
14. Wu, J. et al. Deep-potential enabled multiscale simulation of gallium nitride devices on boron arsenide cooling substrates. *Nat. Commun.* **15**, 2540 (2024).
15. Sun, Z. et al. Investigating thermal transport across the AlN/diamond Interface via the machine learning potential. *Diam. Relat. Mater.* **147**, 111303 (2024).
16. Qi, Z. et al. In-depth insights into crystal orientation and temperature dependence of interfacial thermal transport in diamond/SiC heterostructures by machine learning molecular dynamics. *Int. Commun. Heat. Mass Transf.* **166**, 109231 (2025).
17. Sun, Z. et al. A comprehensive exploration of thermal transport at Cu/diamond interfaces via machine learning potentials. *npj Comput. Mater.* **11**, 359 (2025).
18. Song, K. et al. General-purpose machine-learned potential for 16 elemental metals and their alloys. *Nat. Commun.* **15**, 10208 (2024).
19. Fan, Z. et al. Neuroevolution machine learning potentials: combining high accuracy and low cost in atomistic simulations and application to heat transport. *Phys. Rev. B* **104**, 104309 (2021).
20. Zhang, J. et al. Ultra-wide bandgap semiconductor Ga_2O_3 power diodes. *Nat. Commun.* **13**, 3900 (2022).
21. Sun, Z. et al. Insight into interfacial heat transfer of β-Ga_2O_3/diamond heterostructures via the machine learning potential. *ACS Appl. Mater. Interfaces* **16**, 31666–31676 (2024).
22. Sun, Z. et al. Laser stealth dicing of β-Ga_2O_3: theoretical and experimental studies. *J. Mater. Sci. Technol.* **238**, 303–312 (2025).
23. Sun, Z. et al. A neuroevolution potential for predicting the thermal conductivity of α, β, and ε-Ga_2O_3. *Appl. Phys. Lett.* **123**, 192202 (2023).
24. Wang, X. et al. Dissimilar thermal transport properties in κ-Ga_2O_3 and β-Ga_2O_3 revealed by homogeneous nonequilibrium molecular dynamics simulations using machine-learned potentials. *J. Appl. Phys.* **135**, 065104 (2024).
25. Ning, J. et al. Van der Waals β-Ga_2O_3 thin films on polycrystalline diamond substrates. *Nat. Commun.* **16**, 8144 (2025).
26. Luo, W. et al. Heat transfer enhancement of N-Ga-Al semiconductors heterogeneous interfaces. *Int. J. Heat. Mass Transf.* **244**, 126902 (2025).
27. Zhou, W. et al. Ultrahigh interfacial thermal conductance for cooling gallium oxide electronics using cubic boron arsenide. *Phys. Rev. Appl.* **24**, L031005 (2025).
28. Guo, R., Li, G., Tang, J., Wang, Y. & Song, X. Small-data-based machine learning interatomic potentials for graphene grain boundaries enabled by structural unit model. *Carbon Trends* **11**, 100260 (2023).
29. Chen, B. et al. Machine learning interatomic potential for predicting the thermal properties of uranium nitride. *J. Appl. Phys.* **138**, 205102 (2025).
30. Chen, B. et al. Predicting thermal conductivity of InP via molecular dynamics simulations with machine learning potential. *J. Phys. D Appl. Phys.* **58**, 485105 (2025).
31. Adnan, K. Z., Neupane, M. R. & Feng, T. Thermal boundary conductance of metal–diamond interfaces predicted by machine learning interatomic potentials. *Int. J. Heat. Mass Transf.* **235**, 126227 (2024).
32. Zhang, L., Tian, F., Chen, K., Yan, Z. & Cao, K. Uniaxial stress tuning of interfacial thermal conductance in cubic BAs/4H-SiC heterostructures. *Phys. Rev. Mater.* **9**, 094604 (2025).
33. Liang, T. et al. NEP89: Universal neuroevolution potential for inorganic and organic materials across 89 elements. *arXiv preprint arXiv:2504.21286* (2025).
34. Onn, D., Witek, A., Qiu, Y., Anthony, T. & Banholzer, W. Some aspects of the thermal conductivity of isotopically enriched diamond single crystals. *Phys. Rev. Lett.* **68**, 2806 (1992).
35. Wei, R. et al. Thermal conductivity of 4H-SiC single crystals. *J. Appl. Phys.* **113**, 053503 (2013).
36. Qian, X., Jiang, P. & Yang, R. Anisotropic thermal conductivity of 4H and 6H silicon carbide measured using time-domain thermoreflectance. *Mater. Today Phys.* **3**, 70–75 (2017).
37. Morelli, D. et al. Carrier concentration dependence of the thermal conductivity of silicon carbide. *Inst. Phys. Conf. Ser.* **137**, 313–316 (1994).
38. Jiang, P., Qian, X., Li, X. & Yang, R. Three-dimensional anisotropic thermal conductivity tensor of single crystalline β-Ga_2O_3. *Appl. Phys. Lett.* **113**, 232105 (2018).
39. Abdullaev, A. et al. Thermal conductivity of double polymorph Ga_2O_3 structures. *APL Mater.* **12**, 081108 (2024).
40. Shanks, H., Maycock, P., Sidles, P. & Danielson, G. Thermal conductivity of silicon from 300 to 1400. *K. Phys. Rev.* **130**, 1743 (1963).
41. Gordiz, K. & Henry, A. A formalism for calculating the modal contributions to thermal interface conductance. *N. J. Phys.* **17**, 103002 (2015).
42. Stanley, C. M., Rader, B. K., Laster, B. H., Servati, M. & Estreicher, S. K. The role of interface vibrational modes in thermal boundary resistance. *Phys. status solidi (a)* **218**, 2100111 (2021).
43. Yao, L. et al. Precise thermal dissipation of Ga_2O_3 devices integrated with diamond heat spreading layer. *Mater. Today Commun.* **47**, 113191 (2025).
44. Liu, C., Li, Y. & Wang, C. Thermal characteristics analysis of Ga_2O_3 and GaN devices on different substrates. *Microelectron. J.* **150**, 106266 (2024).
45. Wang, G. & Zhou, Y. Thermal management modeling for β-Ga_2O_3-highly thermal conductive substrates heterostructures. *IEEE Trans. Compon. Packaging Manuf. Technol.* **12**, 638–646 (2022).
46. Kresse, G. & Furthmüller, J. Efficiency of ab-initio total energy calculations for metals and semiconductors using a plane-wave basis set. *Comput. Mater. Sci.* **6**, 15–50 (1996).
47. Kresse, G. & Joubert, D. From ultrasoft pseudopotentials to the projector augmented-wave method. *Phys. Rev. B* **59**, 1758 (1999).
48. Perdew, J. P., Burke, K. & Ernzerhof, M. Generalized gradient approximation made simple. *Phys. Rev. Lett.* **77**, 3865 (1996).
49. Blöchl, P. E. Projector augmented-wave method. *Phys. Rev. B* **50**, 17953 (1994).
50. Wang, V., Xu, N., Liu, J., Tang, G. & Geng, W. VASPKIT: a user-friendly interface facilitating high-throughput computing and analysis using VASP code. *Computer Phys. Commun.* **267**, 108033 (2021).
51. Stukowski, A. Visualization and analysis of atomistic simulation data with OVITO-the open visualization tool. *Model. Simul. Mater. Sci. Eng.* **18**, 015012 (2009).
52. Momma, K. & Izumi, F. VESTA 3 for three-dimensional visualization of crystal, volumetric and morphology data. *J. Appl. Crystallogr.* **44**, 1272–1276 (2011).
53. Chen, C. et al. NepTrain and NepTrainKit: automated active learning and visualization toolkit for neuroevolution potentials. *Computer Phys. Commun.* **317**, 109859 (2025).
54. Xu, K. et al. GPUMD 4.0: a high-performance molecular dynamics package for versatile materials simulations with machine-learned potentials. *Mater. Genome Eng. Adv.* **3**, e70028 (2025).
55. Swartz, E. T. & Pohl, R. O. Thermal boundary resistance. *Rev. Mod. Phys.* **61**, 605 (1989).
56. Dickey, J. & Paskin, A. Computer simulation of the lattice dynamics of solids. *Phys. Rev.* **188**, 1407 (1969).

57. Bell, R. & Dean, P. Atomic vibrations in vitreous silica. *Discuss. Faraday Soc.* **50**, 55–61 (1970).
58. Guo, H., Kong, Y. & Chen, T. Thermal simulation of high power GaN-on-diamond substrates for HEMT applications. *Diam. Relat. Mater.* **73**, 260–266 (2017).

Acknowledgements

This work was funded by the National Natural Science Foundation of China (Grant Nos. 92473102, 52202045, 62004141), the Shenzhen Science and Technology Program (Grant No. JCYJ20240813175906008), the State Key Laboratory of Micro-nano Engineering Science (Grant No. MES202608), and the Open Fund of Hubei Key Laboratory of Electronic Manufacturing and Packaging Integration (Wuhan University) (Grant No. EMPI2025007). The numerical calculations in this paper have been done on the supercomputing system in the Supercomputing Center of Wuhan University.

Author contributions

Z.S. and Z.Q. contributed equally to this work. Z.S.: Writing - original draft, Methodology, Investigation, Software, Conceptualization. Z.Q.: Writing - original draft, Methodology, Investigation, Software. Y.S.: Software, Methodology, Investigation. L.L.: Writing - review & editing. S.L.: Writing - review & editing. W.S.: Writing - review & editing, Investigation, Funding acquisition, Conceptualization. G.W.: Writing - review & editing, Supervision, Project administration, Software, Funding acquisition, Conceptualization.

Competing interests

The authors declare no competing interests.

Additional information

Correspondence and requests for materials should be addressed to Wei Shen or Gai Wu.